Observation of Chirality-Induced Roton-Like Dispersion in a 3D Micropolar Elastic Metamaterial

Yi Chen,* Jonathan L. G. Schneider, Michael F. Groß, Ke Wang, Sebastian Kalt, Philip Scott, Muamer Kadic, and Martin Wegener*

A theoretical paper based on chiral micropolar effective-medium theory suggested the possibility of unusual roton-like acoustical-phonon dispersion relations in 3D elastic materials. Here, as a first novelty, the corresponding inverse problem is solved, that is, a specific 3D chiral elastic metamaterial structure is designed, the behavior of which follows this effective-medium description. The metamaterial structure is based on a simple-cubic lattice of cubes, each of which not only has three translational but also three rotational degrees of freedom. The additional rotational degrees of freedom are crucial within micropolar elasticity. The cubes and their degrees of freedom are coupled by a chiral network of slender rods. As a second novelty, this complex metamaterial is manufactured in polymer form by 3D laser printing and its behavior is characterized experimentally by phonon-band-structure measurements. The results of these measurements, microstructure finite-element calculations, and solutions of micropolar effective-medium theory are in good agreement. The roton-like dispersion behavior of the lowest phonon branch results from two aspects. First, chirality splits the transverse acoustical branches as well as the transverse optical branches. Second, chirality leads to an ultrastrong coupling and hybridization of chiral acoustical and optical phonons at finite wavevectors.

1. Introduction

Phonons are the vibrational eigenstates of the coupled system of atomic nuclei in a crystal.[1] The phonon dispersion relation determines many material properties, for example, the speed of sound, heat conductivity, specific heat, and infrared absorption. In artificial man-made crystals called metamaterials,[2–9] the atoms of ordinary solids are replaced by designed microstructured functional building blocks ("meta-atoms"). This step allows for obtaining unprecedented metamaterial-phonon properties and dispersion relations. For example, chiral transverse acoustical phonons as eigenstates instead of linearly polarized transverse phonons have been realized in chiral elastic metamaterials,[10–12] leading to pronounced acoustical activity,[13–15] the elastic counterpart of optical activity.[16] Unlike for ordinary chiral crystals,[17,18] the size of the effects can be tailored and the operation frequency can be changed by orders of magnitude by the choice of the metamaterial period or lattice constant.

More recently, based on linear chiral micropolar effective-medium elasticity,[19–22] Kishine et al.[23] suggested that extreme chirality could lead to unusual phonon dispersion relations resembling the roton dispersion relation of sound in superfluid helium[24,25] or in Bose Einstein condensates of atoms.[26–30] In the roton dispersion relation,[30] angular frequency ω versus wavenumber k starts with $\omega(k) \propto k$ in the long-wavelength limit ($k \to 0$) and exhibits a maximum (sometimes referred to as the "maxon") at a wavenumber k_{max}, followed by a minimum (the "roton") at a larger wavenumber k_{min}. If the minimum $\omega(k_{min})$ tends to zero frequency, the system approaches an instability (or a soft mode),[26] as also emphasized by Kishine et al.[23] At wavenumbers $k_{max} < k < k_{min}$ in between the maximum and the minimum,

Y. Chen, M. F. Groß, M. Wegener
Institute of Nanotechnology
Karlsruhe Institute of Technology (KIT)
76128 Karlsruhe, Germany
E-mail: yi.chen@partner.kit.edu; martin.wegener@kit.edu

Y. Chen, J. L. G. Schneider, M. F. Groß, K. Wang, S. Kalt, P. Scott, M. Wegener
Institute of Applied Physics
Karlsruhe Institute of Technology (KIT)
76128 Karlsruhe, Germany

K. Wang
National Key Laboratory of Science and Technology on Advanced Composites in Special Environments
Harbin Institute of Technology
Harbin 150001, China

M. Kadic
Institut FEMTO-ST
UMR 6174
CNRS
Université de Bourgogne Franche-Comté (UBFC)
Besançon 25030, France
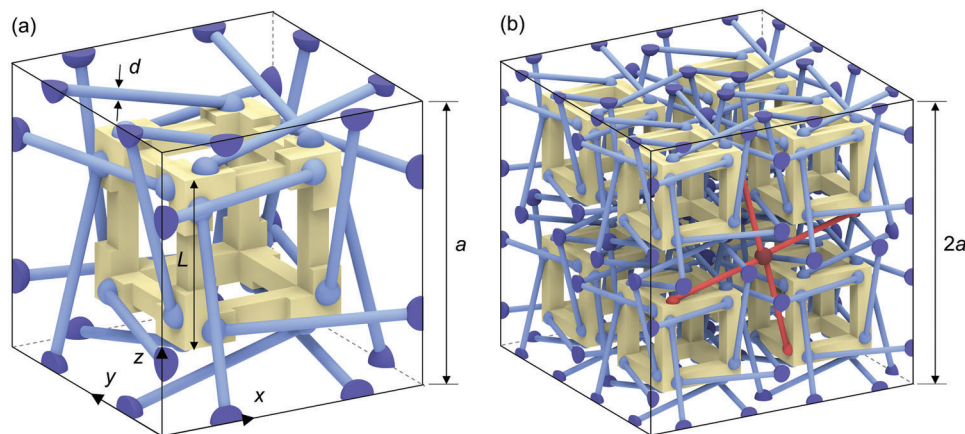
Figure 1. Illustration of the designed 3D chiral metamaterial. a) A cubic unit cell with lattice constant a includes a hollowed-out cube (light-yellow) with side length L and 24 cylindrical rods (light-blue), with diameter d. The 24 half spheres (light-blue) and 24 quarter spheres (dark-blue) serve to connect rods with rods and rods with cubes. All components are made of the same material; colors are for illustration only. This unit cell exhibits no mirror symmetries, but all rotation symmetries of a cube. Further geometrical parameters are indicated in Figure S1 (Supporting Information). A Standard Triangle Language (STL) model is provided in File S1 (Supporting Information). b) $2 \times 2 \times 2$ unit cells of a resulting metamaterial crystal. The rods highlighted in red couple a unit cell not only with nearest-neighboring unit cells but also with neighbors along the face-diagonal directions. Movie S1 (Supporting Information) provides different viewing angles of the same structure.

one obtains a region with negative group velocity, hence effectively negative acoustical refractive index. Conceptually, this negative index can occur over a very wide range of frequencies. Unlike for mechanisms related to local resonances,[2,4] this broadband negative refractive index of the lowest band is not necessarily connected to losses via the Kramers–Kronig relations.[31–33] Kishine et al.[23] predicted that one handedness of the chiral acoustical phonons could exhibit a roton-like behavior, whereas the other handedness would not. This prediction triggered work on obtaining roton-like dispersion relations along paths other than chirality.[34–37]

Here, following along the original lines of using chiral micropolar elasticity,[23] we design 3D elastic microstructures. For simple-cubic crystal symmetry and extreme geometrical parameters, we obtain pronounced acoustical activity and pronounced roton-like behavior of chiral metamaterial phonons. We manufacture corresponding polymer-based 3D samples by 3D laser microprinting and measure their phonon band structures in the ultrasound regime using laser-scanning confocal optical microscopy and laser Doppler vibrometry. We obtain excellent agreement between theory and experiment. These overall results represent a chiral route to roton-like dispersions of the lowest band that is complementary to a different previous (achiral) route based on third-nearest-neighbor interactions.[38–44] There, rotons have resulted from the ultrastrong coupling and hybridization of two different acoustical phonon modes.[34–36] Here, rotons result from the ultrastrong coupling and hybridization of optical and acoustical phonon branches. We emphasize that chirality is a necessary but by far not a sufficient condition for achieving chirality-induced roton-like phonon bands in chiral metamaterials. In fact, pronounced roton-like behavior has not previously been observed in chiral mechanical metamaterials. It is also important that the structure is carefully designed such that the effective material properties are near the edge of the elastic stability regime. After all, the roton minimum can be seen as a precursor for an instability.

2. Metamaterial Design

Figure 1 shows the blueprint of the considered 3D metamaterial structure. It is composed of a single Cauchy-elastic constituent material. Below, we will choose a polymer that can be 3D printed. Colors in Figure 1 are for illustration only. The construction of the metamaterial crystal in Figure 1 starts from a simple-cubic periodic arrangement of cubes (light-yellow) with period or lattice constant a. The cube's side length is L. We remove unnecessary parts of the cubes to reduce their mass and to ease the manufacturing (see Figure S1, Supporting Information, for detailed geometrical parameters). Each cube has three translational degrees of freedom plus three rotations around three orthogonal axes. Cauchy elasticity captures the translations,[45] whereas the rotations are specific for micropolar elasticity.[19] These six degrees of freedom per metamaterial unit cell support not only acoustical but also optical phonon modes. The achiral cubes are connected by a chiral arrangement of cylindrical rods (light-blue), with diameter d. These rods allow the cubes to actually explore all their degrees of freedom. Importantly, the rods also couple the degrees of freedom of different cubes. This aspect leads to the mentioned hybridization of acoustical and optical phonon modes (see below). Note that the rods not only couple a cube to its six nearest neighbors along the three principal directions, but also directly to the twelve neighbors along the cube's face-diagonal directions (cf. rods highlighted in red in Figure 1b). This coupling is important because chiral behavior (equivalent to a "k-linear term" in wavenumber space[13]) can generally be interpreted as a nonlocal effect.[19] Therefore, pronounced chiral behavior requires pronounced non-local chiral couplings. It is clear that the force or energy that is necessary to displace or rotate the cubes with respect to their rest positions decreases with decreasing diameter, d, of the rods. In particular, the bending stiffness of a long cylindrical rod or beam scales according to $\propto d^4$.[45] Indeed, we will see below that the targeted roton-like phonon dispersion relations only occur for sufficiently small ratios
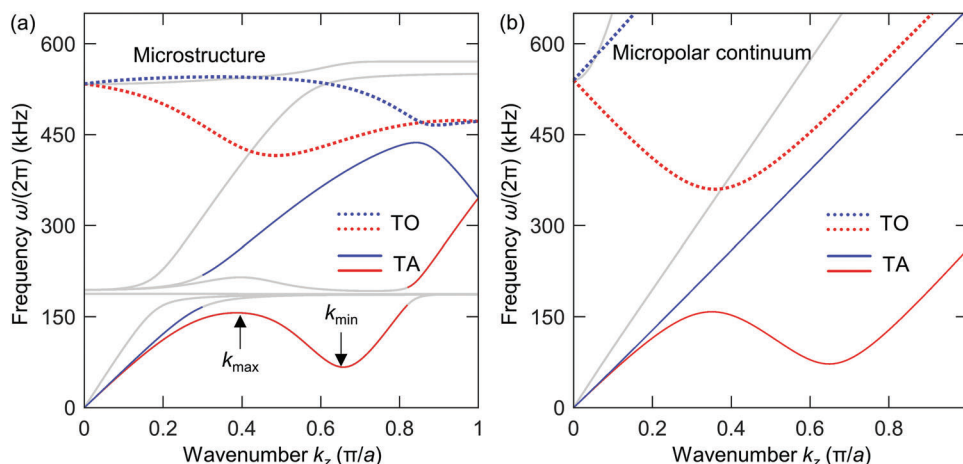
Figure 2. Chirality-induced roton-like dispersion relations. a) Calculated metamaterial (cf. Figure 1) phonon dispersion relation for wave vectors along the k_z direction. Chirality leads to a pronounced frequency splitting between the two transverse acoustical (TA) branches (red and blue solid curves) and between the two transverse optical (TO) branches (red and blue dashed curves). The first TA branch (solid red curve) exhibits a pronounced roton minimum at $k_{min} \approx 0.65\ \pi/a$ due to a chirality-induced ultrastrong avoided crossing with one of the TO modes (dashed red curve). The geometrical parameters $L/a = 0.6$, $d/a = 0.04$, and $a = 185\ \mu m$ used here are also targeted in the below experiments. We choose $E = 4.19$ GPa, $\nu = 0.4$, and $\rho = 1140$ kg m^{-3} for the Young's modulus, Poisson's ratio, and mass density of the constituent polymer. b) As (a), but using a micropolar continuum model (see Note S1, Supporting Information). Animations of the TA and TO phonon eigenstates for different wavenumbers are provided as Movies S2–S5 (Supporting Information).

$d/a \ll 1$. Finally, the small spheres (light-blue and dark-blue) serve to connect rods to rods and rods to cubes. These spheres are not essential in our design, but they help to obtain a well-defined structure. They also improve the fault tolerance with respect to fabrication imperfections, for example in case that the ends of two rods are unintentionally slightly displaced in 3D space. The resulting 3D metamaterial crystal shown in Figure 1 has three axes with fourfold rotational symmetry, four axes with three-fold rotational symmetry, no center of inversion, no mirror planes, and no rotation-reflection symmetries but still obeys time-reversal symmetry. Therefore, by symmetry, the phonon dispersion relation obeys $\omega_n(\pm k, 0, 0) = \omega_n(0, \pm k, 0) = \omega_n(0, 0, \pm k)$, with band index $n = 1, 2, ...$ and for finite wavenumbers $k \in [-\pi/a, \pi/a]$ within the first Brillouin zone.

Metamaterial–phonon dispersion relations for the architecture defined in Figure 1, obtained by finite-element calculations (see the Experimental Section), are depicted in **Figure 2**a. In addition, we plot in Figure 2b phonon bands derived from a micropolar continuum model of the designed metamaterial (see Note S1 for details, Supporting Information). Here, we consider Bloch-periodic boundary conditions for an infinite 3D periodic metamaterial (i.e., the "bulk" case) and for wavevectors along either of the three equivalent cubic axes. More complete tours through the 3D Brillouin zone are shown in Figure S2 (Supporting Information). We find that the lowest phonon band in Figure 2 develops a roton-like minimum for sufficiently small values of d/a, connected to a region of backward waves for $k_{max} < k < k_{min}$. This roton minimum results specifically from chirality. Chirality splits the two otherwise degenerate transverse acoustical (TA) phonon modes, leading to acoustical activity.[14] Likewise, chirality also splits the two transverse optical (TO) phonon branches. This splitting shifts the minimum of the optical phonon dispersion away from $k = 0$ to a finite wavenumber, leading to negative group velocity of one of the branches. A similar behavior has previously been

discussed for chiral electromagnetic metamaterials.[46] This optical branch hybridizes with the acoustical phonons and admixes the negative-group-velocity behavior to the acoustical phonons. Altogether, chirality thereby induces the roton-like behavior of the lowest band by ultrastrong coupling. At small wavenumbers, the eigenmodes of the TA branches are circularly polarized and dominated by translations of the cubes (see Movies S2 and S3, Supporting Information). In sharp contrast, even at small wavenumbers, the eigenmodes of the TO branches exhibit pronounced rotations rather than just translations of the cubes. The central cube simultaneously rotates around the x-axis and the y-axis (see Movies S2, Supporting Information). This behavior is in agreement with that of the eigenstates for the TO branches derived from the micropolar continuum theory [see Equation (S24), Supporting Information]. At larger wavenumbers, TA and TO phonons hybridize, translating the rotations to the TA-phonon like modes and leading to the roton-like behavior. Indeed, for wavenumbers in the negative-group-velocity region as well as for the roton minimum, we find a combination of translations and rotations of the cubes, as expected for micropolar elasticity (see Movies S4 and S5, Supporting Information). The rotations connected to the couple stress in micropolar elasticity are the main reason for the negative energy flow connected to the negative group velocity (see Figure S3 and Note S2, Supporting Information).

In the limit of $d/a \to 0$, the roton minimum at angular frequency $\omega(k_{min})$ approaches zero in the sense of $\omega(k_{min})/\omega(k_{max}) \to 0$ (see Figure S4, Supporting Information). Therefore, the roton minimum can be interpreted as a precursor for an instability at finite wavenumbers, which was previously pointed out by Kishine et al.[23] We note in passing that zero-frequency modes at finite wavenumbers have recently also been shown for metamaterials involving other mechanisms.[47] The flat bands around 200 kHz frequency in Figure 2a are due to mass-and-spring type local

**ADVANCED
SCIENCE NEWS**

www.advancedsciencenews.com

**ADVANCED
FUNCTIONAL
MATERIALS**

www.afm-journal.de
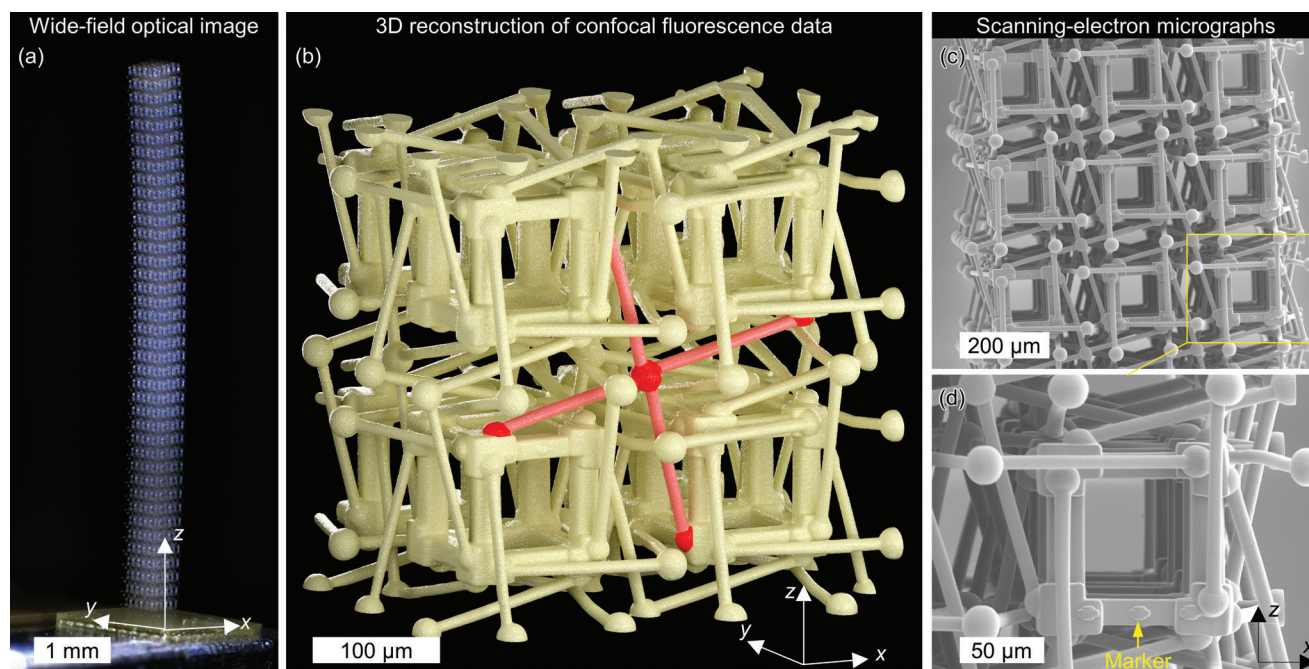
Figure 3. Gallery of measured images of manufactured chiral micropolar metamaterial samples. a) Wide-field optical microscopy image of an entire sample with $3 \times 3 \times 40$ unit cells. b) 3D reconstruction of a part of a sample based on autofluorescence of the constituent polymer taken with a scanning confocal fluorescence optical microscope (LSM 980, Zeiss). Colors are for illustration only. One cross composed of rods is highlighted in red (cf. Figure 1b). c,d) Side-view scanning electron microscopy images of part of the sample. d) For zoomed-in view of the region in (c) highlighted by the yellow rectangle. The yellow arrow indicates one of the markers used for tracking.

resonances of the heavy cubes together with the compliant rods (cf. Figure 1). As local resonances are not accounted for in micropolar elasticity, no detailed agreement between the microstructure and the micropolar-effective-medium calculations shown in Figure 2 can be expected at around 200 kHz and above. Furthermore, the effective-medium model is not expected to match the microstructure results for large wavenumbers. As can be seen, the two TA phonon branches calculated for the microstructure are degenerate at the edge of the Brillouin zone because of the four-fold rotational symmetry of the metamaterial around its principal direction.[9,11,12] The effective-medium model cannot capture this degeneracy, because any effective-medium model ignores the periodicity of the metamaterial. In other words, there is no counterpart of the Brillouin-zone edge in reciprocal space for the effective-medium model. Nevertheless, the overall agreement, especially for the lowest bands, is good. This means that we have identified a specific metamaterial microstructure (cf. Figure 1) that leads to the roton-like dispersion relations predicted by Kishine et al.[23] on the basis of micropolar elasticity. They considered tetragonal crystal symmetry, whereas we consider cubic symmetry herein.

3. Experimental Results

Next, we test the design shown in Figure 1 experimentally. In these experiments, we consider samples with finite cross section rather than the fictitious bulk case considered so far. Caution has to be exerted because micropolar elasticity breaks the scale invariance of Cauchy elasticity, which means that the metamaterial properties are generally expected to depend on the number of

unit cells therein. In additional calculations (see Figure S5, Supporting Information), we find that the roton-like behavior survives for 3×3 unit cells within the metamaterial-beam cross section and above. We manufacture 3D metamaterial beams with $3 \times 3 \times 40$ unit cells as illustrated in Figure 1 by standard 3D laser microprinting (Nanoscribe, Photonics Professional GT) as used several times previously by us.[11,12] The printed material is composed of an acrylate (Nanoscribe, IP-S), the elastic properties of which are well approximated by a Young's modulus of $E = 4.19$ GPa, a Poisson's ratio of $v = 0.4$, and a mass density of $\rho = 1140$ kg m^{-3}. These parameters have already been used in the calculations shown in Figure 2 and in previous publications by us on other laser-printed metamaterials.[11,12,36] More details of the fabrication are provided in the Experimental Section. Selected scanning-electron micrographs of samples under different viewing angles and with different magnifications are shown in **Figure 3**. The metamaterial samples come close to the blueprint ideal (cf. Figure 1). In addition, one can see cross-shaped markers on cubes (cf. Figure 3d). These markers are important for the measurements to be described next.

The phonon band-structure experiments on these samples are simple conceptually, yet demanding in detail. We excite the metamaterial beam, glued onto an aluminum cuboid, by a piezoelectric transducer to which we apply a time-harmonic voltage signal with variable frequency. The transducer mainly induces transverse (x- and y-direction, cf. Figure 3a) displacement components with respect to the metamaterial-beam axis. We optically image the sample from the side by using confocal optical laser microscopy in the back-scattering mode, combined with digital image cross-correlation
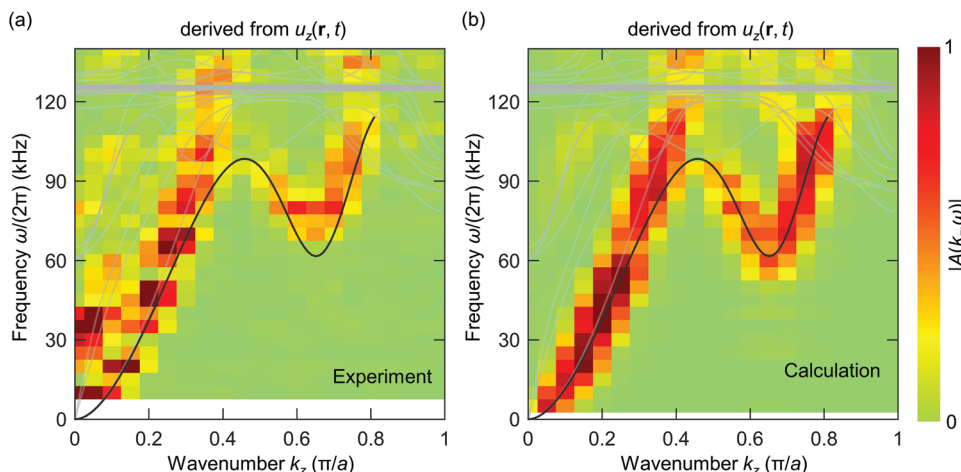
Figure 4. Comparison between experiment and calculations. a) Amplitude $|A(k_z,\omega)|$ plotted on a false-color scale, derived from the measured displacement $u_z(\mathbf{r},t)$ along the metamaterial-beam axis (cf. Figure 3), versus phonon wavenumber and frequency. The solid curves are numerically calculated phonon dispersion relations for the same 3×3 cross section of the metamaterial beam, but for infinitely many unit cells along the z-direction. The lowest band exhibiting the roton-like behavior is shown in black, all other bands are shown in gray. b) Amplitude $|A(k_z,\omega)|$ as in (a), but from numerical calculations of the same finite metamaterial beam composed of $3 \times 3 \times 40$ unit cells as in (a). The solid curves are the same as in a). Corresponding measured and calculated results obtained from the other two displacement components ($u_x(\mathbf{r},t)$ and $u_y(\mathbf{r},t)$) are shown in Figure S8 (Supporting Information).

analysis to obtain the two lateral components, $u_x(\mathbf{r}, t)$ and $u_z(\mathbf{r}, t)$, of the displacement-vector field $\mathbf{u}(\mathbf{r}, t) = (u_x(\mathbf{r}, t), u_y(\mathbf{r}, t), u_z(\mathbf{r}, t))$ in real space and real time. In addition, we use Doppler vibrometry to obtain the third component, $u_y(\mathbf{r}, t)$ (for details see the Experimental Section and Notes S3 and S4, Supporting Information). Along these lines, we achieve localization errors of just a few nm for all three components at variable frequencies up to $\omega/(2\pi) = 200$ kHz.[36,48] Fourier-transformation with respect to time t and Fourier transformation with respect to the real space coordinates $z = ma$, with integer $m = 1, 2, ...40$, leads to the complex-valued response function $A(k_z,\omega)$ with modulus $|A(k_z,\omega)|$, the maxima of which reflect the dispersion relation $\omega(k_z)$. The spacing of points in the first Brillouin zone with $|k_z| \leq \pi/a$ is $\Delta k_z = (2\pi/a)/40$. It is important to note that the positions of the maxima of $|A(k_z,\omega)|$ only depend on the metamaterial-beam dispersion relation $\omega_n(k_z)$, whereas the height of the maxima also depends on the coupling between the piezoelectric transducer and the metamaterial beam. This means that parts of the dispersion relation can be missing, which is clearly undesirable. Therefore, we have tailored the region of the metamaterial near the substrate surface such that all relevant modes become clearly visible. Details of the interface-region design are provided in Figure S7 (Supporting Information).

Figure 4a exhibits measurements of $|A(k_z,\omega)|$ derived from the displacement component $u_z(\mathbf{r}, t)$. Results from the other two components are similar (see Figure S8, Supporting Information). The solid curves are calculations using Bloch-periodic boundary conditions along the beam axis, assuming zero damping (as above). These curves as well as the finite-element simulations for the same finite-size metamaterial beam shown in Figure 4b (see the Experimental Section), agree well with the experiments. In Figure 4b, we have accounted for inner damping of the constituent material by introducing a finite imaginary part of the Young's modulus of the constituent material given by 10% of its real part (see above). In Figure 4, for the

lowest phonon branch, $\omega_1(k_z)$, a maximum followed by a region of negative slope and a minimum are clearly visible. We have targeted this roton-like behavior with our design. The depth of the roton minimum (or inverse peak-to-valley ratio) is given by $\omega_1(k_{min})/\omega_1(k_{max}) \approx 0.63$. In principle, the roton minimum could be brought closer to $\omega(k_{min})/\omega(k_{max}) = 0$ by further reducing the ratio d/a in the metamaterial structure (cf. Figure S4, Supporting Information), thereby approaching an instability at the roton-minimum wavenumber k_{min} (see above). However, such yet smaller ratios of d/a are presently not accessible at sufficient sample quality by the used laser-printing approach. From $|A(k_z,\omega)|$ in Figure 4, one can also see part of the longitudinal-like phonon branch $\omega_3(k_z)$ at small wavenumbers k_z. The many other phonon branches (see gray curves) either result from local resonances (see above) or from back-folding of the bulk dispersion relation due to the finite lateral extent of the metamaterial beam in the xy-plane. These branches are not visible in the $|A(k_z,\omega)|$ data in Figures 4 because the used excitation does not couple to the corresponding phonon eigenmodes. The amplitude map $|A(k_z,\omega)|$ in Figure 4a obtained from the experiment is limited in resolution with respect to the frequency and the wavenumber, mainly due to the finite length of the metamaterial beam along the phonon propagation direction in the experiment, but also due to the finite frequency steps used. Therefore, the rather small frequency splitting between the two chiral TA branches, i.e., the lowest two bands, is not resolved in the low-frequency range. This observation is consistent with the numerical calculations show in Figure 4b. However, the much larger frequency splitting between the two chiral TA bands above around 95 kHz is clearly visible from both, experiment and theory.

4. Conclusion

We realized 3D chiral micropolar metamaterials exhibiting roton-like dispersion relations of the lowest phonon band specifically

resulting from chirality. The roton minimum can be seen as a precursor of an instability at finite wavenumbers that arises in the limit of very thin rods connecting the cubes within the metamaterial. The chiral character of the corresponding phonons means that the center of mass of a metamaterial unit cell rotates around its rest position, clockwise or counter-clockwise. This rotation somewhat resembles Landau's interpretation[24] of the roton in superfluid helium that gave rise to the name "roton." However, apart from the similarities in the dispersion relations and the eigenmodes of the two systems, superfluid helium and elastic metamaterials, the underlying physics is distinct. It might thus be interesting to design metamaterials that more closely resemble the physics of superfluid helium, e.g., in that they exhibit a temperature-dependent phase transition. It also remains to be seen whether roton-like behavior can be achieved in 2D rather than in 3D mechanical metamaterials.

5. Experimental Section

Finite Element Calculations: All numerical calculations were performed by using the commercial finite element software COMSOL Multiphysics. Specifically, the linear elasticity equation

$$\frac{E}{2(1+\nu)(1-2\nu)}\nabla\left(\nabla\cdot\mathbf{u}_{k,n}(\mathbf{r})\right)$$
$$+\frac{E}{2(1+\nu)}\nabla^2\mathbf{u}_{k,n}(\mathbf{r}) = -\rho\omega_{k,n}^2\mathbf{u}_{k,n}(\mathbf{r}) \quad (1)$$

is solved for finding the eigenfrequencies $\omega_{k,n}$ and the displacement eigenmodes $\mathbf{u}_{k,n}(\mathbf{r})$ corresponding to the Bloch wavevector $\mathbf{k}$ and integer band index n. We set the Young's modulus, the Poisson's ratio, and the mass density of the constituent polymer material to be $E = 4.19$ GPa, $\nu = 0.4$, and $\rho = 1140$ kg m^{-3}, respectively.[48] For phonon bands of an infinite bulk metamaterial (cf. Figure 2 and Figures S2 and S3, Supporting Information), we apply Bloch-period boundary conditions at all six surfaces of the cubic unit cell shown in Figure 1a. For a metamaterial beam with a finite cross section (cf. Figure 4 and Figure S5, Supporting Information), Bloch-periodic conditions are only applied along the beam-axis direction. All other boundaries are treated as traction free.

Time-harmonic responses of the metamaterial beam (cf. Figure 4b) are also obtained by using COMSOL Multiphysics with the following equation

$$\frac{E}{2(1+\nu)(1-2\nu)}\nabla\left(\nabla\cdot\mathbf{u}_{\omega}(\mathbf{r})\right)$$
$$+\frac{E}{2(1+\nu)}\nabla^2\mathbf{u}_{\omega}(\mathbf{r}) = -\rho\omega^2\mathbf{u}_{\omega}(\mathbf{r}) \quad (2)$$

where ω represents the angular frequency of the excitation and $\mathbf{u}_{\omega}(\mathbf{r})$ is the resultant displacement-vector field. We impose a time-harmonic transverse displacement, $\mathbf{u} = (1, 0, 0)\exp(-i\omega t)$, at the bottom of the metamaterial beam. All other boundaries are set to be traction free. To account for the effects of viscous damping, a damping ratio of 10% is introduced for the constituent polymer, i.e., the imaginary part of the Young's modulus of the polymer is set to be 10% of its real part. We note that the applied displacement at the bottom of the metamaterial beam is purely transverse in the numerical calculations, while the piezo transducer in the experiment also generates a weak longitudinal displacement along the beam axis. In the measurement results (cf. Figure 4a), a weak amplitude for $|A(k_z,\omega)|$ is observed for the longitudinal band, while the longitudinal band is completely suppressed in calculations (cf. Figure 4b).

Metamaterial Sample Fabrication with Laser Printing: The sample fabrication generally follows the previous publications on microscopic metamaterials.[5,6,35] A commercial 3D laser printer (Professional GT,

Nanoscribe GmbH) with a 25× objective lens (numerical aperture NA = 0.8, Carl Zeiss) was used. Metamaterial beam samples were printed using a commercial liquid photoresist (IP-S, Nanoscribe GmbH) within the dip-in printing mode. A printing laser power of 27.5 mW and a laser focus scanning speed of 0.145 m s^{-1} were used.

The metamaterial beam was modeled in the commercial software COMSOL Multiphysics. Compensations to the geometric model were considered to correct for the discrepancies between the actually printed sample and the targeted ideal sample. These discrepancies result from the ellipsoidal laser focus instead of an ideal spherical focus.[5,6] Because of multiple overhanging rods in the metamaterial, the geometry was split into different parts, and these parts were printed sequentially. The metamaterial beam was printed on a glass substrate, covered by a thin sacrificial layer (polyvinyl alcohol, around 150 nm in thickness), with its beam axis parallel to the glass substrate. The hatching distance and slicing distance were chosen to be 200 nm and 300 nm, respectively. A bottom plate was directly printed at one end of the metamaterial beam with the printing parameters of 50 mW for the laser power, 0.140 m s^{-1} for the focus scanning speed, 500 nm and 1.5 μm for the hatching distance and slicing distance, respectively. The plate eases the mount of the metamaterial beam onto a piezo transducer. More details about the printing setting can be found in the GWL-files that are published in [https://dx.doi.org/10.35097/945].

After completing the light exposure, the sample was first immersed in propylene glycol methyl ether acetate and ethanol for 20 min each to remove excess photoresist. Afterward, the sacrificial layer was dissolved in warm water (around 40 °C) to enable lifting-off the sample from the substrate, followed by air drying for 1 h.

Experimental Setup and Single-Frequency Excitation: The home-built measurement setup consists of a confocal optical laser scanning microscope with an integrated laser Doppler vibrometer in Mach–Zehnder configuration and was used in previous work.[48] Elastic waves were excited in the sample with a piezoelectric transducer (PL055.31 PICMA, Physik Instrumente) driven with an amplified time-harmonic voltage to which the data acquisition of the confocal imaging mode and the laser Doppler vibrometry mode were synchronized to. This ensures the correct recovery of the temporal phase of the displacement field $\mathbf{u}(\mathbf{r}, t) = (u_x(\mathbf{r}, t), u_y(\mathbf{r}, t), u_z(\mathbf{r}, t))$, which is sampled at 40 regions of interest (ROI) along the beam axis. Since the metamaterial sample exceeds the field of view of the setup, the sample was manipulated by *xyz*-translation stages using piezo-inertia drives (Physik Instrumente, Q-545).

For every excitation frequency from 10 to 150 kHz, each ROI was measured. The frequency increment is 5 kHz. Subsequently, the three displacement components were extracted from the raw data. From the generated image data, the in-plane u_x and u_z displacement components were derived using digital image cross-correlation analysis, while the out-of-plane component u_y was calculated using in-phase and quadrature demodulation of the laser-Doppler signal. A more detailed description can be found in the Supporting Information as well as in a previous work.[48]

Supporting Information

Supporting Information is available from the Wiley Online Library or from the author.

Acknowledgements

Conflict of Interest

The authors declare no conflict of interest.

Data Availability Statement

The data that support the findings of this study are openly available in [KIT] at [https://dx.doi.org/10.35097/945].

Keywords

[1] C. Kittel, P. McEuen, *Introduction to Solid State Physics*, Wiley, New York **1996**.

[2] Z. Liu, X. Zhang, Y. Mao, Y. Zhu, Z. Yang, C. T. Chan, P. Sheng, *Science* **2000**, *289*, 1734.

[3] G. W. Milton, *The Theory of Composites*, Cambridge University Press, Cambridge **2002**.

[4] X. Fang, J. Wen, L. Cheng, D. Yu, H. Zhang, P. Gumbsch, *Nat. Mater.* **2022**, *21*, 869.

[5] R. Zhu, X. N. Liu, G. K. Hu, C. T. Sun, G. L. Huang, *Nat. Commun.* **2014**, *5*, 5510.

[6] S. A. Cummer, J. Christensen, A. Alù, *Nat. Rev. Mater.* **2016**, *1*, 16001.

[7] C. Coulais, D. Sounas, A. Alù, *Nature* **2017**, *542*, 461.

[8] M. Kadic, G. W. Milton, M. van Hecke, M. Wegener, *Nat. Rev. Phys.* **2019**, *1*, 198.

[9] Y. Chen, T. Frenzel, Q. Zhang, M. Kadic, M. Wegener, *Phys. Rev. Mater.* **2021**, *5*, 025201.

[10] X. Liu, G. Huang, G. Hu, *J. Mech. Phys. Solids* **2012**, *60*, 1907.

[11] T. Frenzel, M. Kadic, M. Wegener, *Science* **2017**, *358*, 1072.

[12] T. Frenzel, J. Köpfler, E. Jung, M. Kadic, M. Wegener, *Nat. Commun.* **2019**, *10*, 3384.

[13] D. L. Portigal, E. Burstein, *Phys. Rev.* **1968**, *170*, 673.

[14] Y. Chen, M. Kadic, S. Guenneau, M. Wegener, *Phys. Rev. Lett.* **2020**, *124*, 235502.

[15] Y. Chen, M. Kadic, M. Wegener, *Proc. Math. Phys. Eng. Sci.* **2021**, *477*, 20200764.

[16] L. D. Barron, *Molecular Light Scattering and Optical Activity*, Cambridge University Press, Cambridge **2004**.

[17] A. S. Pine, *Phys. Rev. B* **1970**, *2*, 2049.

[18] K. Ishito, H. Mao, Y. Kousaka, Y. Togawa, S. Iwasaki, T. Zhang, S. Murakami, J. Kishine, T. Satoh, *Nat. Phys.* **2023**, *19*, 35.

[19] A. C. Eringen, *Microcontinuum Field Theories*, Springer, New York **1999**.

[20] Z. Rueger, R. S. Lakes, *Phys. Rev. Lett.* **2018**, *120*, 065501.

[21] D. R. Reasa, R. S. Lakes, *Phys. Rev. Lett.* **2020**, *125*, 205502.

[22] Y. Chen, T. Frenzel, S. Guenneau, M. Kadic, M. Wegener, *J. Mech. Phys. Solids* **2020**, *137*, 103877.

[23] J. Kishine, A. S. Ovchinnikov, A. A. Tereshchenko, *Phys. Rev. Lett.* **2020**, *125*, 245302.

[24] L. Landau, *Phys. Rev.* **1941**, *60*, 356.

[25] R. P. Feynman, *Phys. Rev.* **1954**, *94*, 262.

[26] P. Nozières, *J. Low Temp. Phys.* **2004**, *137*, 45.

[27] N. Henkel, R. Nath, T. Pohl, *Phys. Rev. Lett.* **2010**, *104*, 195302.

[28] H. Godfrin, M. Meschke, H. Lauter, A. Sultan, H. M. Böhm, E. Krotscheck, M. Panholzer, *Nature* **2012**, *483*, 576.

[29] D. Petter, G. Natale, R. M. W. van Bijnen, A. Patscheider, M. J. Mark, L. Chomaz, F. Ferlaino, *Phys. Rev. Lett.* **2019**, *122*, 183401.

[30] H. Godfrin, K. Beauvois, A. Sultan, E. Krotscheck, J. Dawidowski, B. Fåk, J. Ollivier, *Phys. Rev. B* **2021**, *103*, 104516.

[31] D. Forcella, C. Prada, R. Carminati, *Phys. Rev. Lett.* **2017**, *118*, 134301.

[32] P. Kinsler, M. W. McCall, *Phys. Rev. Lett.* **2008**, *101*, 167401.

[33] M. I. Stockman, *Phys. Rev. Lett.* **2007**, *98*, 177404.

[34] Y. Chen, M. Kadic, M. Wegener, *Nat. Commun.* **2021**, *12*, 3278.

[35] R. Fleury, *Nat. Phys.* **2021**, *17*, 766.

[36] J. A. I. Martínez, M. F. Groß, Y. Chen, T. Frenzel, V. Laude, M. Kadic, M. Wegener, *Sci. Adv.* **2021**, *7*, m2189.

[37] Y. Chen, K. Wang, M. Kadic, S. Guenneau, C. Wang, M. Wegener, *Commun. Phys.* **2023**, *6*, 75.

[38] L. Brillouin, *Wave Propagation in Periodic Structures*, Dover Publications, New York **1953**.

[39] K. Wang, Y. Chen, M. Kadic, C. Wang, M. Wegener, *Commun. Mater.* **2022**, *3*, 35.

[40] Z. Zhu, Z. Gao, G. Liu, Y. Ge, Y. Wang, X. Xi, B. Yan, F. Chen, P. P. Shum, H. Sun, Y. Yang, *New J. Phys.* **2022**, *24*, 123019.

[41] Q. Wu, P. Shivashankar, X. Xu, Y. Chen, G. Huang, *J. Compos. Mater.* **2022**, *54*, 771.

[42] J. Cui, T. Yang, M. Niu, L. Chen, *J. Appl. Mech.* **2022**, *89*, 111005.

[43] Y. Chen, M. A. A. Abouelatta, K. Wang, M. Kadic, M. Wegener, *Adv. Mater.* **2023**, *35*, 2209988.

[44] K. Wang, Y. Chen, M. Kadic, C. Wang, M. Wegener, *Acta Mech. Sin.* **2023**, *39*, 723020.

[45] K. F. Graff, *Wave Motion in Elastic Solids*, Courier Corporation, North Chelmsford, MA **2012**.

[46] J. B. Pendry, *Science* **2004**, *306*, 1353.

[47] A. Bossart, R. Fleury, *Phys. Rev. Lett.* **2023**, *130*, 207201.

[48] M. Groß, J. Schneider, Y. Wei, Y. Chen, S. Kalt, M. Kadic, X. Liu, G. Hu, M. Wegener, *Adv. Mater.* **2023**, *35*, 2211801.